University of Massachusetts Amherst
ScholarWorks@UMass Amherst

Masters Theses   Dissertations and Theses

2017

Experimental Study on Viscoelastic Fluid-Structure Interactions

Anita Anup Dey
University of Massachusetts Amherst

Recommended Citation

www.manaraa.com

EXPERIMENTAL STUDY ON VISCOELASTIC FLUID-STRUCTURE INTERACTIONS

A Thesis Presented

by

ANITA ANUP DEY

EXPERIMENTAL STUDY ON VISCOELASTIC FLUID-STRUCTURE INTERACTIONS

A Thesis Presented

by

ANITA ANUP DEY

Approved as to style and content by:

_____

Jonathan P. Rothstein, Chair

_____

Yahya Modarres-Sadeghi, Member

_____

Matthew Lackner, Member

_____

Sundar Krishnamurty, Department Head
Mechanical and Industrial Engineering

ABSTRACT

EXPERIMENTAL STUDY ON VISCOELASTIC FLUID-STRUCTURE INTERACTIONS

MAY 2017

ANITA ANUP DEY

B.E., SARDAR PATEL COLLEGE OF ENGINEERING

M.S.M.E., UNIVERSITY OF MASSACHUSETTS AMHERST

Directed by: Professor Jonathan P. Rothstein

It is well known that when a flexible or flexibly-mounted structure is placed perpendicular to the flow of a Newtonian fluid, it can oscillate due to the shedding of separated vortices at high Reynolds numbers. If the same flexible object is placed in non-Newtonian flows, however, the structure's response is still unknown. The main objective of this thesis is to introduce a new field of viscoelastic fluid-structure interactions by showing that the elastic instabilities that occur in the flow of viscoelastic fluids can drive the motion of a flexible structure placed in its path. Unlike Newtonian fluids, the flow of viscoelastic fluids can become unstable at infinitesimal Reynolds numbers due to the onset of a purely elastic flow instability. This instability occurs in the absence of nonlinear effects of fluid inertia and the Reynolds number of the flows studied here are in the order of 10^{-4}. When such an elastic flow instability occurs in the vicinity of a flexible structure, the fluctuating fluid forces exerted on the structure grow large enough to cause a structural instability which in turn feeds back into

the fluid resulting in a flow instability. Nonlinear periodic oscillations of the flexible structure are observed which have been found to be coupled to the time-dependent growth and decay of viscoelastic stresses in the wake of the structure. Presented in this thesis are the results of an investigation of the interaction occurring in the flow of a viscoelastic wormlike micelle solution past a flexible rectangular sheet. The structural geometries studied include: flexible sheet inclinations at 20°, 45° and 90° and flexible sheet widths of 5mm and 2.5mm. By varying the flow velocity, the response of the flexible sheet has been characterized in terms of amplitude and frequency of oscillations. Steady and dynamic shear rheology and filament stretching extensional rheology measurements are conducted in order to characterize the viscoelastic wormlike micelle solution. Bright field images show the deformation of the flexible sheet during an unstable oscillation while flow-induced birefringence images highlight the viscoleastic fluid stresses produced in the wake of the flexible sheet.

TABLE OF CONTENTS

LIST OF FIGURES

CHAPTER 1

INTRODUCTION

1.1 Non-Newtonian fluids

Non-Newtonian fluids are a significant component in daily life showing many interesting characteristics, the most important being that they may behave like an elastic Hookean solid or a viscous Newtonian fluid or a complex combination of the two, depending on the timescale in which they are investigated. These fluids are often called viscoelastic fluids. The combination of viscosity and elasticity is imparted by the physical nature of the macromolecules in these fluids, which may be present in the form of high molecular weight polymers, self-assembled wormlike micelles or suspensions of micron or nanoscale particles. As a flexible polymer coil or wormlike micelle stretches within a flow field, it is deformed out of its equilibrium random configuration. An elastic restoring force results, driving the polymer or micelle back toward its entropically favorable equilibrium state [1]. This leads to a characteristic fluid timescale known as the relaxation time,

$$\lambda = \frac{\eta}{G},\tag{1.1}$$

which describes the time required for the polymer coil or wormlike micelle to relax from a deformed state back to its equilibrium configuration. Here η is the viscosity and G is the elastic modulus of the fluid. For these fluids, Newton's law of viscosity no longer holds. They are therefore described as non-Newtonian fluids. Thus, the residence time of a fluid in a flow must also be considered to understand the viscoelastic

1

fluid's response. The relative importance of elasticity in a flow is described by a Deborah number which is the ratio of the relaxation time of the fluid to a characteristic deformation timescale,

$$De = \frac{\lambda}{t_{flow}}. \tag{1.2}$$

If the deformation timescale is large in comparison to the relaxation time of the fluid, $De \ll 1$, then the polymer coil has ample time to relax back to equilibrium and the fluid will behave like a Newtonian fluid. If the relaxation time is much longer than the deformation timescale in the flow, $De \gg 1$, then the fluid will react like an elastic Hookean solid. The behavior of the fluid between these two extremes is quite rich.

Viscoelastic wormlike micelle solutions are currently being used extensively as rheological modifiers in consumer products such as paints, detergents, pharmaceuticals, lubricants and emulsifiers where careful control of the fluid properties are required. In addition, micelle solutions have also become important in a wide range of applications including agrochemical spraying, inkjet printing, turbulent drag reduction and enhanced oil recovery where they are often used as a polymer-free fracture fluid for stimulating oil production [2–4]. A fundamental understanding of the behavior of these complex fluids in different flow regimes is therefore extremely important to a host of industries. Techniques for the analysis and control of the flow of complex fluids require accurate determination of material properties as well as the ability to understand and predict changes that occur within the materials as they are subjected to the flow conditions encountered in industrial and commercial applications. Shear and extensional rheometers provide an excellent framework for investigating the behavior of these complex fluids because the flow kinematics tends to be simple. Additionally, these rheological measurements can shed light on the dynamics of wormlike micelle solutions in complex flows and phenomena such as elastic flow instabilities, which commonly occur in many of the industrial and commercial applications mentioned above. A number of studies of the nonlinear rheology and the behavior of these complex fluids

2
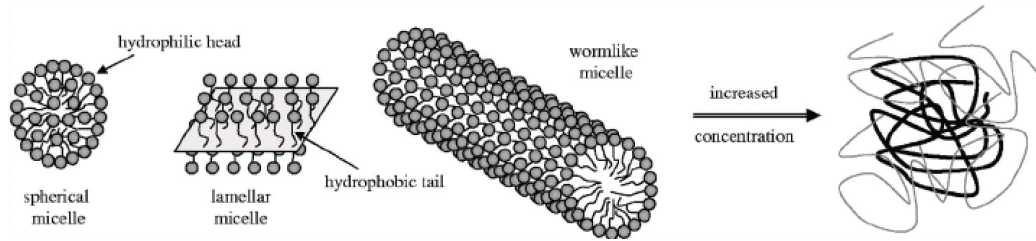
Figure 1.1. Various morphologies of wormlike micelles which impart viscoelasticity

in strong flows have recently been published. Surfactants are amphiphilic molecules which have both a bulky hydrophilic head, which is often charged, and a relatively short and slender hydrophobic tail typically consisting of an 8-20 carbon atom chain. Above their critical micelle concentration (CMC), surfactant molecules in water will spontaneously self-assemble into large aggregates known as micelles to minimize the exposure of their tails to water [5–7]. In oil, reverse micelles are formed where instead the head-groups are shielded from the oil [8,9]. As seen in Figure 1.1, these large aggregates can form into a number of different complex shapes including spherical and wormlike micelles, vesicles and lipid bilayers [10]. The morphology of the aggregates depends on the size of the surfactant head group, the length and number of tails, the charge on the surfactant, the salinity of the solution, temperature, and the flow conditions [5,10]. We are most interested in wormlike micelle because, as suggested by their pseudonym 'living polymers', wormlike micelles display many of the same viscoelastic properties of polymers. However, although both wormlike micelle solutions and polymer solutions can be viscoelastic, wormlike micelles are physically quite different from polymers. Whereas the backbone of a polymer is covalently bonded and rigid, wormlike micelles are held together by relatively-weak physical attractions and as a result are continuously breaking and reforming with time. In an entangled network, both individual polymer chains and wormlike micelles can relieve stress through reptation driven by Brownian motion [6]. However, unlike polymeric fluids, wormlike micelle solutions have access to a number of stress relief mechanisms in ad-

3

dition to reptation. Wormlike micelles can relieve stress and eliminate entanglement points by either breaking and reforming in a lower stress state [7] or alternatively by creating a temporary branch point which allows two entangled micelles to pull right through each other thereby eliminating the entanglement point and relieving stress in what has become known as a 'ghost-like' crossing [11]. Additionally, the constant re-organization of the network structure results in several interesting phenomenon when subjected to strong flows. Under all but the most extreme conditions, these solutions' large viscosities lead to a vanishingly small Reynolds number,

$$Re = \frac{\rho V L}{\mu} \tag{1.3}$$

where ρ is the fluid density, U is the flow velocity, L is the characteristic length scale and μ is the fluid viscosity. In all of the experiments presented in this work, the Reynolds number is of order 10^{-4}. An interesting feature of wormlike micelles is their mechanism of mechanical failure under an applied stress. Flow curves have shown these solutions to be shear thinning [7], and strain hardening [12], however these two non-Newtonian behaviors do not predict their method of failure. In extensional flow, when a fluid filament experiences a large enough stress, the value of which is independent of strain rate it fails dramatically at its mid plane. This behavior has been observed most recently by Rothstein et al. [13], and is believed to be caused by a scission of individual micelle chains. This type of dramatic failure can manifest itself as instabilities in not just extensional flows, but complex flows as well. For example, the flow around a sphere contains regions of shear as the fluid passes around the circumference, as well as extension in the wake of the sphere. Given that the fluid is known to be shear thinning as well as extensionally thickening, the combination of these qualities and the complex flow field yields some interesting results. Chen and Rothstein [14] observed that above a critical Deborah number a new class of elastic instabilities, related to the rupture of these micellar solutions in the extensional flow

4

present in the wake of a sphere occurred. By measuring the flow fields with PIV and FIB they were able to explore the kinematics of the flow. Similar instabilities have also been observed by Belmonte et al. [15].

1.2 Newtonian fluid-structure interactions

When a flexible or flexibly mounted structure is placed in the path of fluid flow, the fluid exerts a force on the structure which causes the structure to deform. This deformation of the structure in turn modifies the fluid forces exerted by the fluid flow. This leads to a coupling between structural motion and the fluctuating fluid forces. This constitutes a fluid-structure interaction (FSI). The field of FSI has many applications in harnessing wind energy, novel energy extraction methods and biomedical engineering. The fundamental studies on FSI for Newtonian fluid have been collected in the form of several books and review papers (e.g., [16–22]). Of all these studies, here we will focus on a model FSI problem: Vortex-Induced Vibration (VIV).

VIV of a flexibly-mounted rigid cylinder with a circular cross-section placed in fluid flow and free to oscillate in the cross-flow direction, i.e., the direction perpendicular to the oncoming flow, has become the canonical problem in FSI. Work by several investigators has helped elucidate the fundamentals of VIV [16,21–27]. Large-amplitude oscillations occur when the frequency of vortex formation is relatively close to the natural frequency of the structure. Then the frequency of vortex shedding can be entrained and become equal to the frequency of the structural crossflow vibrations, this wake-body resonance condition is referred to as lock-in. Substantial differences exist when the rigid cylinder is also allowed to move in the inline direction, the direction parallel to the oncoming flow [28,29]. Inclusion of the inline motion leads to significant changes in hydrodynamic forces acting on the rigid cylinder, depending on the phase difference between the inline and the crossflow vibrations [30,31].

5

The case of a long flexible cylinder in a cross-flow has been considered only recently due to its complexities. These complexities are associated with the distributed interaction between the fluid and the flexible body, including the difficulty to pinpoint the region where the fluid excites the body, and identifying the mechanisms of energy redistribution along the span. Detailed laboratory experiments on flexible structures placed in flow have provided information on the amplitude of vibration, excited frequencies and structural wave numbers [32]. For long flexible cylinders, contrary to the case of rigid cylinders, the phase difference between the inline and crossflow displacements can vary along the span, leading to diverse trajectories along the structure [33–35]. A dominant mechanism has been identified in the interaction between a flexible circular cylinder undergoing free vibrations in sheared crossflow and the vortices forming in its wake: energy is transferred from the fluid to the body under a resonance condition, which occurs within a well-defined region of the span, dominated by counterclockwise, figure-eight orbits [30].

In all the cases of FSI described above, the fluid was Newtonian and the flow was at moderate to high Reynolds numbers, $Re > 50$. In these inertial-dominated flows, the motion of the cylinder was driven by the shedding of vortices which separate from the cylinder and shed from its wake. There are, however, a whole class of flows in which the Reynolds number is vanishingly small, inertia plays essentially no role and yet the flow can become unstable. In these cases, the presence of high molecular weight polymers or wormlike micelles can make the fluids elastic. The combination of fluid elasticity and mean curvature of the streamlines has been shown to destabilize the flow and lead to the onset of elastically-driven flow instabilities [36]. In this study, we present results that show that these instabilities can drive the motion of a flexible structure placed in its flow path.

6

1.3 Objective

The goal of this thesis is to study fluid-structure interaction (FSI) phenomena in which the fluid is a non-Newtonian viscoelastic fluid and the structure is flexible. FSI has been studied extensively for structures in contact with Newtonian fluid where the shedding of separated vortices at high Reynolds numbers can drive the motion of a flexibly-mounted or flexible structure. There are, however, no studies in the literature of FSI for viscoelastic fluids. Unlike Newtonian fluids, the flow of viscoelastic fluids can become unstable even at very small Reynolds numbers in the order of 10^{-4} seen in literature for flow past stationary objects. This flow instability can provide a periodic driving force on flexible structures, resulting in a new class of FSI problems. This phenomenon has not yet been studied. FSI of viscoelastic fluids is an open problem with the potential to have a transformative impact on the field of fluid-structure interactions. In our study, we have observed structural instabilities caused by instabilities of a non-Newtonian viscoelastic fluid.

Viscoelastic fluids such as polymer melts and solutions, micelles solutions and suspensions are encountered in a variety of industries and applications critical to modern day economics. A fundamental understanding of how these viscoelastic fluids interact with structures can have significant influence on a number of very different applications ranging from polymer processing to health care. An example is the use of carbon fiber reinforced polymer composites. With the push to higher fuel economy standards, reducing the weight of cars and airplanes while maintaining their structural integrity is highly desirable. Carbon fiber reinforced composite parts are formed by driving a polymer resin through a woven carbon fiber mat. At the high flow rates desired to make this process economically competitive, the viscoelastic polymeric fluid can experience an elastic flow instability. This flow instability can drive the motion of the carbon fiber matrix, which could cause undesired effects such as fiber packing, inhomogenous fiber distribution, and even failure of the fibers. Here the FSI

7

between a flowing viscoelastic fluid and one or more elastic solid fibers is critically important to the success of an injection molded part. The proposed research can also have an impact on a number of biological systems. Due to the presence of proteins and polypeptides, many biological fluids are viscoelastic. As an example, when the viscoelasticity of middle ear effusions becomes too large, it can impair the ability of beating cilia that line the walls of the inner ear to remove the fluid [37], leading to ear infections. Understanding the FSI between beating cilia and the mucous-like excretions could eventually lead to better strategies for preventing ear infections.

A large body of work exists on low Reynolds number swimmers. In the case of swimming, a two-way coupling between flow and structure is not needed: the structure pushes the fluid around it in order to propel itself. A number of recent numerical and experimental studies have investigated the importance of viscoelasticity on the propulsion of different model micro-organisms [38–41]. In all of these studies, the structure is externally activated to move and the fluid's motion is a result of the structure's motion. What we propose to study is concerned with the cases where the viscoelastic fluid undergoes instability, when the structure is not moving. This flow instability then forces the structure to move, which in turn will modify the fluid motion. This two-way coupling between the viscoelastic fluid instability and the structural instability (response) is the focus of this thesis.

8

CHAPTER 2

EXPERIMENTAL SETUP

2.1 Flow geometry

In order to observe viscoelastic FSI, a deformable structure was mounted within a rectangular flow cell and exposed to a crossflow of a viscoelastic wormlike micelle solution. A flexible natural rubber sheet having a length of 50 mm, width 5 mm and thickness 0.3 mm served as the deformable structure. The flexible sheet was clamped at both ends to the walls at the midplane of the rectangular channel and aligned perpendicular to the flow direction. The flexible sheet had an elastic modulus of E = 101 kPa and its natural frequency was measured to be $f_N = 0.15$ Hz from pluck tests of the mounted sheet in air. This measurement closely matches the predictions for a beam with clamped ends. The flow cell was made of acrylic so it would be transparent and had an internal cross section of 50 mm × 50 mm and a length of 450 mm. In order to avoid containment effects, the flexible sheet was placed such that a sheet to channel width of at least 5:1 can be maintained. In this way, the greatest shear gradient experienced by the test fluid will be along the flexible sheet and not the bounding channel walls. The viscoelastic wormlike micelle solution used here was composed of 50 mM of a cationic surfactant cetyltrimethyl ammonium bromide (CTAB) and 25 mM of sodium salicylate (NaSal) in deionized distilled water. A study of the shear and transient extensional rheology of this solution has been discussed in the fluid rheology section.

To minimize the driving pressure fluctuations, a positive displacement piston pump was fabricated and used to produce a precisely controllable, constant flow

9
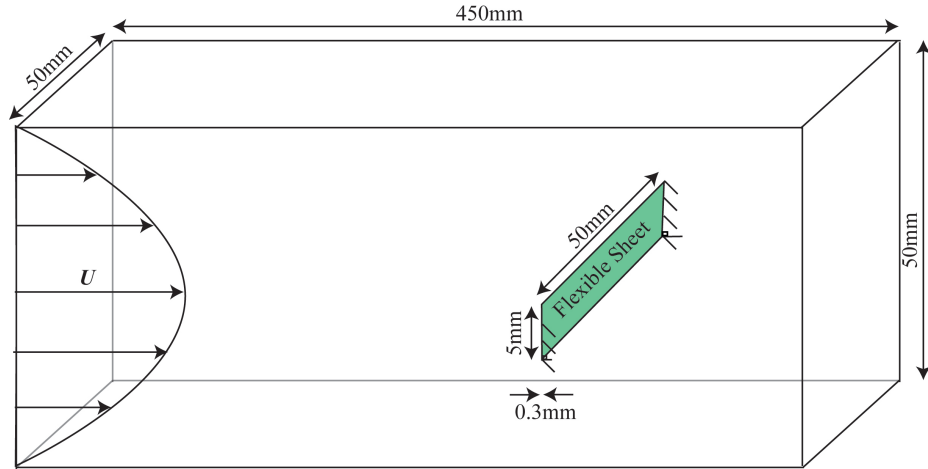
Figure 2.1. Schematic diagram of the geometry used to study the flow of wormlike micelle solution past a flexible sheet

rate through the channel. The piston motion was controlled with addressable micro-staging, capable of a flow rate resolution of 4 mm^3/s. Due to the precision of the pumping system, the flow velocity can be accurately controlled, allowing for a repeatable and accurate interrogation of the test fluid using any number of measurement techniques. In this study, the flow velocity was varied from 0 to 14 mm/s to explore the flexible sheet deformation, fluid-structure interaction and flow induced birefringence as a function of the average flow velocity.

2.2   Structural deformation tracking

In order to quantitatively measure the deformation of the flexible sheet during the flow of the test fluid, discrete points were marked along the length of the sheet as shown in Fig. 2.2. During the test, the motion of the flexible sheet was captured using a high speed camera (Phantom V4.2). Using a high speed camera allowed videos to be recorded at 100 frames per second. The captured high resolution videos were then used as an input in a tracking software (Tracker), which located and tracked the motion of discrete points and provided the displacement time histories at each point for each frame. For every test, velocity of the test fluid was step-increased

10
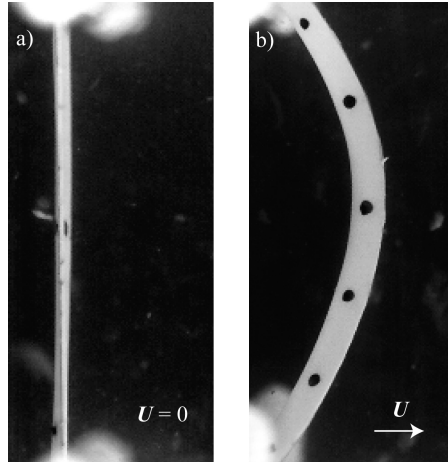
Figure 2.2. Flexible sheet position at (a) rest and (b) under flow conditions.

from zero to a specific flow velocity, wherein the flexible sheet deformed from the no-flow position to a deformation having a static displacement. In the experiments conducted for this study, the flexible sheet showed only the first mode of excitation in the unstable oscillations. Therefore, only the midsection point on the sheet was inputed into the tracking software and this was sufficient to gain information regarding the amplitude and frequency of oscillations. For each time history, a minimum of 180 seconds of data was collected once the flexible sheet achieved a steady mean displacement. Additionally, in order to illustrate the complex deformation undergone by the flexible sheet for each cycle of oscillation, bright field images were captured using a Nikon D70 digital camera at small time increments within a single oscillation cycle for various flow velocities. These sets of images were critical in determining the total stress experienced by the flexible sheet based on the total deformation of the sheet profile visible in the bright field images. This total stress was in fact applied by the viscoelastic fluid flowing past the flexible sheet. Thus, the bright field images helped in relating the deformation of the flexible sheet with the stresses developed in the viscoelastic fluid.

11

2.3 Flow-induced birefringence (FIB)

The refractive index of a wormlike micelle varies depending on whether the light passes parallel or normal to the micelles backbone. By passing light of a known polarization state and frequency through a fluid sample and measuring the resulting change in polarization state, flow-induced birefringence takes advantage of this fact to measure the deformation of the micelle. Under all flow conditions, this technique can at least qualitatively elucidate the regions of large stress in a flow. In the limit of small deformations, an optical train can be built up using Mueller calculus, and a value of the micellar deformation can be calculated from a stress-optic coefficient. Flow-induced birefringence measurements have been used quite extensively to examine both steady and transient flows of and wormlike micelles [14,42–45].

A monochromatic light source was used to illuminate the flow between crossed polarizers. A Nikon D70 digital camera was used to capture the birefringent patterns in the wormlike micelle solution generated by the flow for each linear polarizer configuration. Due to the extreme deformation the micellar network undergoes at high Deborah numbers, data analysis becomes impractical because the birefringence quickly goes through orders. As such, for the purpose of this study, the full field FIB technique is used only qualitatively to highlight the deformation; it is a visualization tool to aid the observer.

2.4 Fluid rheology

2.4.1 Sample preparation

The test fluid was composed of wormlike micelle solution assembled from 50 mM of cationic surfactant cetyltrimethylammoniun bromide (CTAB) (MP Biomedicals) and 25 mM of sodium salicylate (NaSal) (Fisher Scientific) in deionized water. This solution is well above the critical micelle concentration, which for CTAB in pure water is CMC = 0.9 mM and is again significantly lower in the presence of salt [5].

The CTAB was dissolved in aqueous NaSal solution on a hot plate with a magnetic stirring bar. During mixing, a moderately elevated temperature was applied to reduce viscosity and aid in uniform mixing. After the solutions were fully dissolved, approximately 20-30 minutes, they were allowed to settle at room temperature for at least 24 hours before any experiments were performed to allow air bubbles introduced during mixing to rise out of solution. At the concentrations used, the wormlike micelle solution is concentrated and entangled with significant number of entanglement points per chain [5].

When analyzing and presenting the experimental data, the relaxation times and viscosities were adjusted to their values at a reference temperature of $T_{ref} = 25°C$ using time-temperature superposition with a shift factor, a_T, defined by the Arrhenius equation [46].

$$a_T = exp\left[- \frac{\triangle \bar{H}}{R}\left[\frac{1}{T} - \frac{1}{T_{ref}}\right]\right] \qquad (2.1)$$

Within the temperature range of our experiments, the Arrhenius form of the time-temperature superposition shift factor was found to be in good agreement with the rheological data for each of the wormlike micelle solutions tested, however, because of the sensitivity of the underlying wormlike micelle structure to temperature, every effort was made to maintain the fluid temperature to within plus or minus a few tenths of a degree for all of the experiments presented herein. Alternatively, the shift factor may be calculated from the Williams-Landel Ferry equation given by

$$log a_T = \frac{-c_1^0(T - T_{ref})}{c_2^0 + (T - T_{ref})} \qquad (2.2)$$

In either case, the time-temperature superposition principle was found to be a valid method of accounting for small differences in laboratory temperature.

13
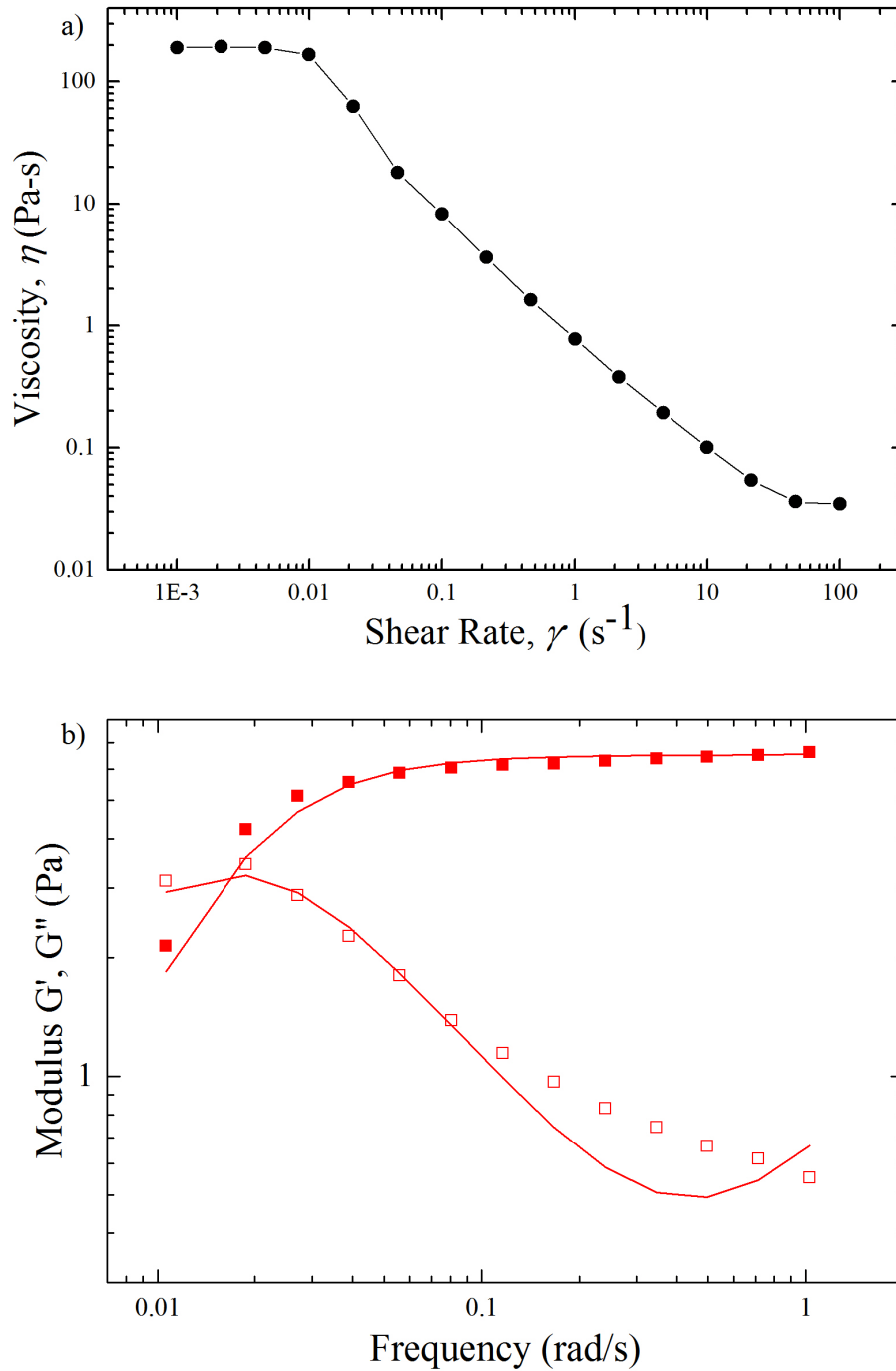
Figure 2.3. Steady and dynamic shear rheology data of the 50mM CTAB/25mM NaSal wormlike micelle solution. (a) shows the viscosity as a function of shear rate. In (b), the ■ symbols represent the storage modulus, G', the □ symbols represent the loss modulus, G'', and the solid lines represent the predictions of a two mode Maxwell model as a function of frequency.

2.4.2 Shear rheology

The steady and dynamic shear rheology of the test fluid was characterized using a stress-controlled rheometer (TA instruments, AR2000) with a $6cm/2°$ cone-and-plate geometry. The micelle solution was loaded and allowed to equilibrate for several minutes. The samples were not pre-sheared. In Figure 2.3(b), the storage modulus, G', and loss modulus, G'', of the CTAB-NaSal wormlike micelle solutions are plotted as a function of angular frequency, ω.

The CTAB-NaSal solution has a Maxwell relaxation time of $\lambda = 47s$ and a zero shear viscosity of $\eta_0 = 200Pas$. The deviation of the rheological data from the predictions of the two mode Maxwell model observed at large angular frequencies in Figure 2.3 correspond to the Rouse-like behavior of the micelle between entanglement points [47] and can be used to determine both the breakup time, λ_{br}, and the reptation time, λ_{rep}, of the wormlike micelle chains. In the fast breaking limit $\lambda_{rep} \ll \lambda_{br}$, Cates showed that the breakup and reptation time could be related to the measured value of the Maxwell relaxation time through $\lambda = \sqrt{\lambda_{br}\lambda_{rep}}$ [48]. Additionally, the theoretical mesh size $\zeta_m = (kT/G_0)^{1/3}$ [49,50] can be determined in order to gain some information about the proximity of entanglement points and the density of the wormlike micelle mesh. The wormlike micelle solution used in this study has breakup and reptation times of 2s and 52.6s respectively and theoretical mesh size of 8.6×10^{-9}. In Figure 2.3(a), the steady shear viscosity, η, is plotted as a function of shear rate, $\dot{\gamma}$. At small shear rates and angular frequencies, the micelle solutions have a constant zero shear rate viscosity. As the shear rate is increased, the fluid begins to shear thin. At a critical shear rate, the viscosity drops precipitously approaching a slope of $\eta \propto \gamma^{-1}$.

2.4.3 Extensional rheology

Wormlike micelle solutions have been the subject of many experiments in extensional flow in recent years. Most recently, Rothstein et al. [51] have studied the effects of pre-shear on the extensional viscosity of solutions of varying concentrations. A filament stretching extensional rheometer (FiSER) capable of imposing a homogeneous uniaxial extension rate, $\dot{\varepsilon}$, on a fluid filament placed between its two endplates was used to make simultaneously measurements of the evolution in the force and the mid-point radius, R_{mid}. In a detailed force balance of the filament stretching rheometer, Szabo [52] showed that the principal elastic tensile stress difference generated within the filament could be calculated from the total force measured by the load cell, F_z, if the weight of the fluid, the surface tension and the inertia of the fluid are taken into account

$$\langle \tau_{zz} - \tau_{rr} \rangle = \frac{F_z}{\pi R_{mid}^2} + \frac{1}{2} \frac{\rho g(\pi L_0 R_0^2)}{\pi R_{mid}^2} - \frac{\sigma}{R_{mid}} + \frac{1}{2} \frac{\rho(\pi L_0 R_0^2)\ddot{L}_z}{\pi R_{mid}^2} \qquad (2.3)$$

where σ is the surface tension of the fluid, ρ is the density of the fluid, and $\ddot{L}_z$ is the acceleration of the endplate. For strain hardening fluids, the contributions of surface tension and gravity to the force balance in eq.2.3 are only significant at small strains or strain rates [53]. The last term of eq.2.3 is due to the fluid inertia and is negligibly small for the present experiments. The principal elastic tensile stress can be further broken down into contributions from the wormlike micelle and its Newtonian solvent,

$$\langle \tau_{zz} - \tau_{rr} \rangle = \triangle \tau_e + 3\eta_s \dot{\varepsilon} \qquad (2.4)$$

where η_s is the solvent viscosity of the fluid. The transient extensional viscosity of polymeric fluids in homogenous uniaxial extension can thus be written as

$$\eta_{ext}^+ = \frac{\langle \tau_{zz} - \tau_{rr} \rangle}{\dot{\varepsilon}} = 3\eta_s + \frac{\triangle \tau_e}{\dot{\varepsilon}} \qquad (2.5)$$

16
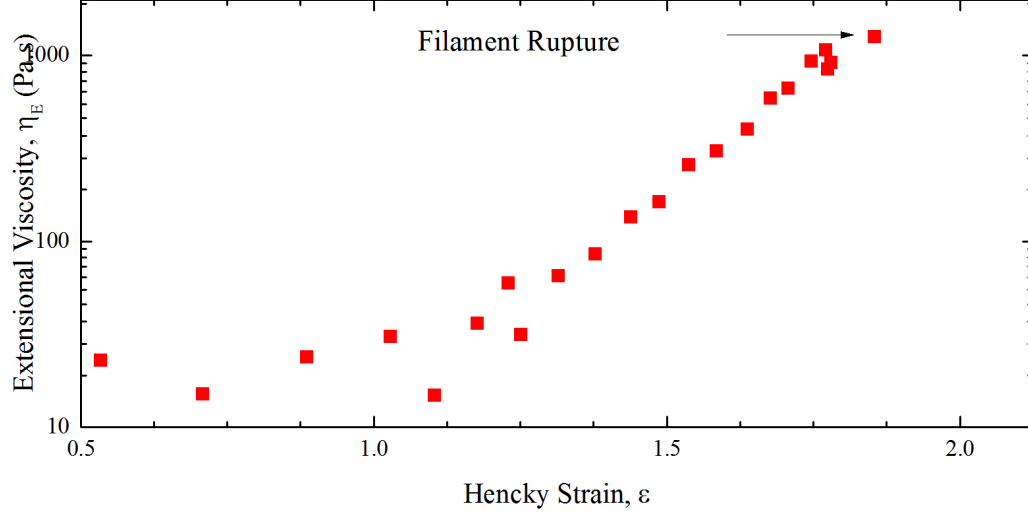
Figure 2.4. Representative plot of transient filament stretching rheometry experiments for the 50mM CTAB/25mM NaSal wormlike micelle solution at $Wi = 288$. The symbols represent the elastic contribution to the tensile stress difference as a function of Hencky strain. The experiment ends abruptly upon the rupture of the fluid filament.

and nondimensionalized with the zero shear rate viscosity to form the Trouton ratio.

$$T_r = \langle \tau_{zz} - \tau_{rr} \rangle / \eta_0 \dot{\varepsilon} = \eta_{ext}^+ / \eta_0 \tag{2.6}$$

The deformation imposed upon the fluid filament can be described in terms of a Hencky strain, $\varepsilon = 2ln(R_{mid}/R_0)$ where R_0 is the initial midpoint radius of the fluid filament. The strength of the extensional flow is characterized by the Weissenberg number, $Wi = \lambda \dot{\varepsilon}$, which is the product of the characteristic relaxation time of the fluid, λ, and the extension rate, $\dot{\varepsilon}$. The Weissenberg number is a measure of the relative importance of elastic to viscous stresses in a flow. For a detailed description of the extensional rheometer used in these experiments see Rothstein [12]. The extensional rheology of the solution tested have been previously investigated and published by Bhardwaj et al. [13,51] and Rothstein [12]. However, for completeness, filament stretching stretching experiments were conducted for the test fluid used in this study. A representative plot of the elastic tensile stress, $\triangle \tau_e$, of the 50/25mM CTAB-NaSal

17
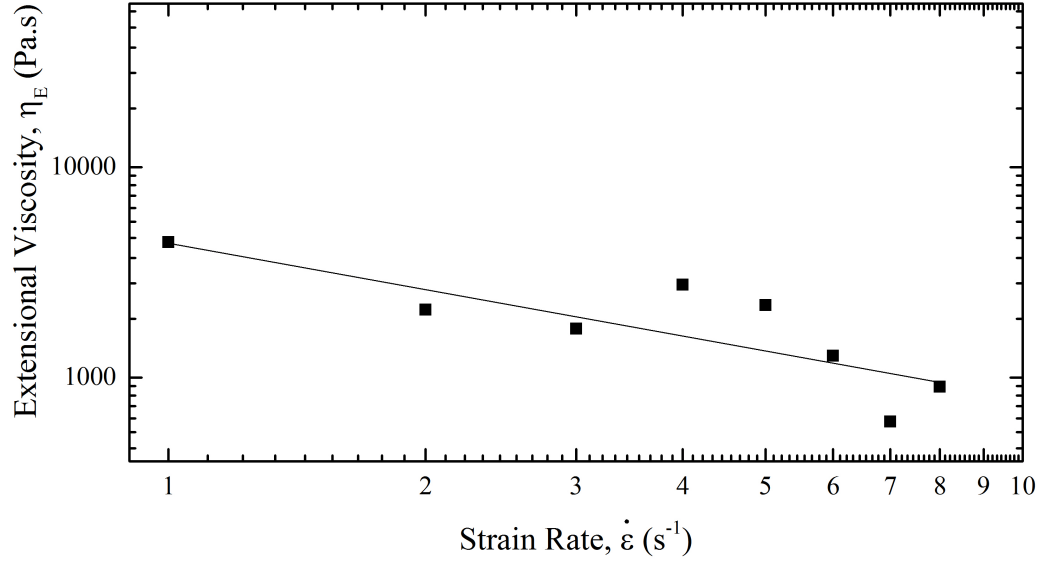
Figure 2.5. The maximum extensional viscosity reached before filament rupture as a function of strain rate for the 50mM CTAB/25mM NaSal wormlike micelle solution.

as a function of Hencky strain for a Weissenberg number of $Wi = 288$ is presented in Fig. 2.4. The elastic tensile stress is found to increase monotonically with increasing Hencky strain and demonstrate reasonably strong strain hardening achieving a final elastic tensile stress, $\triangle\tau_e = 7.5kPa$ at $\varepsilon \cong 1.8$. At large extension rates, $Wi \gg 1$, the fluid filaments were all found to rupture. For all of the experiments that ended with a filament rupture, the final maximum elastic stress that was achieved in the fluid filaments of each solution was found to be constant independent of extension rate [13]. Owing to the constant elastic tensile stress, the extensional viscosity is found to decrease linearly with increasing imposed extension rate, $\eta_E \propto \dot{\varepsilon}^{-1}$ as seen in Fig. 2.5. It has been hypothesized that the tensile stress of rupture corresponds to the maximum stress that the micelles can withstand before they begin to fail en masse [12].The dynamics of the filament rupture have been captured with high-speed photography in the past and the interested reader is referred to Chen and Rothstein [14] or Bhardwaj et al. [13] for details.

18

CHAPTER 3

RESULTS

3.1   Sheet displacement time histories

A series of measurements were made over a range of flow velocities where the maximum Reynolds number of $Re = 3.5 \times 10^{-4}$ was attained. Reynolds number is defined as, $Re = \rho U w / \eta_0$ where ρ is the density of the fluid, U is the flow velocity, w is the width of the sheet, and η_0 is the zero shear rate viscosity. The Re signifies the strength of inertial effects in a flow. As Re is very small, these experiments are in the Stokes flow regime and the inertial flow effects can be neglected. At zero flow velocity, the sheet is undisturbed and aligned perpendicular to the flow direction as seen in Fig. 3.1. As the cross flow is applied, the sheet is bent in the flow direction. Here we observe that in addition to the induced curvature along the length of the sheet that can be observed from the front view in Fig. 3.1, the low flexural rigidity of the sheet results in a secondary curvature across the sheet that can be observed from the side view in Fig. 3.1. The resulting cross-sectional profile is 'C' shaped. At low flow velocities, where the Weissenberg number is small, the flow of the wormlike micelle solution remains stable and, as seen in Fig. 3.1, the static deflection of the sheet grows with increasing average flow speed. As the flow velocity is increased beyond a critical velocity and a corresponding critical Weissenberg number, the flow of the wormlike micelle solution becomes unstable and this in turn affects the stability of the flexible sheet displacement. At this stage, the flexible sheet does not have a constant displacement, but rather begins to oscillate about its stretched position. As was the case for the flow of wormlike micelle solutions past circular cylinders and

19
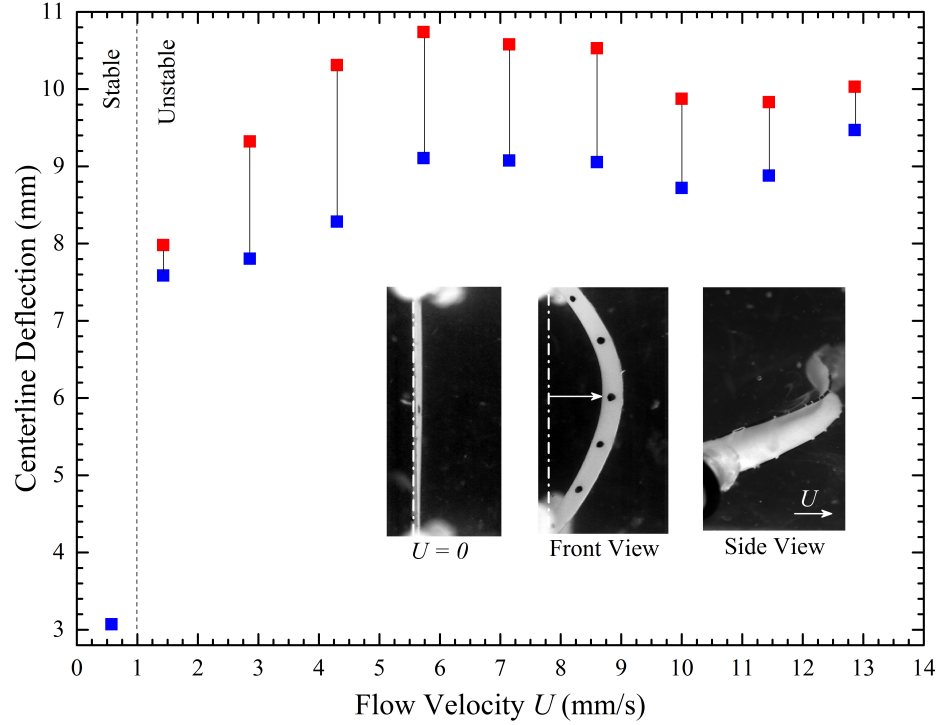
Figure 3.1. Bifurcation diagram of the center line deflection of the flexible sheet versus the flow velocity.

spheres [14,54], the flow instability originates as a slow growth and fast decay of extensional stress in the wake of the flexible sheet.

The bifurcation diagram of Fig. 3.1 shows the maximum and minimum deformations of the flexible sheet versus flow velocity. Below $U_{crit} = 1.43$ mm/s, the flow is stable and the structure undergoes a static deflection but does not oscillate. The Wi at this point corresponds to,

$$Wi_{crit} = \lambda \frac{U_{crit}}{H} = 47s \frac{1.43mm/s}{5mm} = 13.4 \tag{3.1}$$

Above U_{crit}, a periodic response is observed. Just beyond the bifurcation point, the maximum displacement of the flexible sheet increases linearly with flow velocity until a velocity of $U = 6$mm/s, beyond which, the maximum sheet deflection reaches a plateau and remains more or less unchanged for all flow velocities tested. On the

20
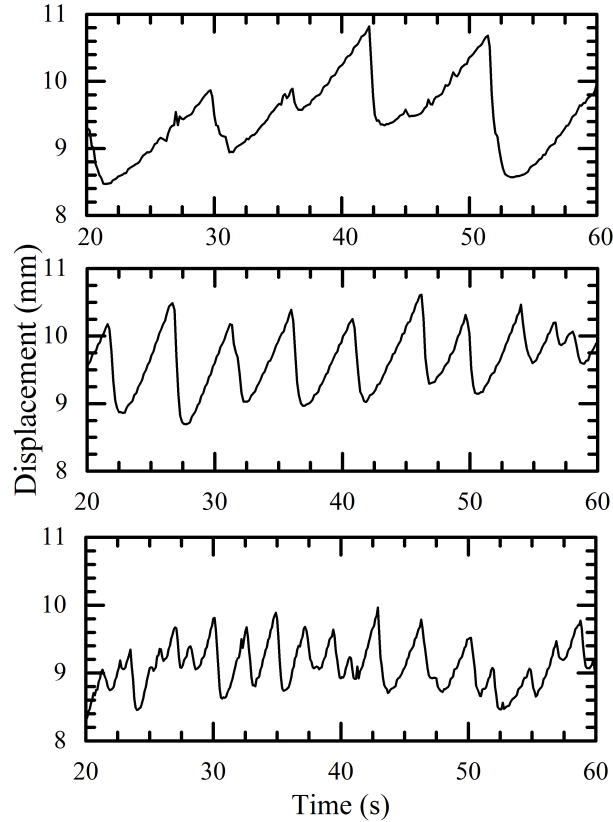
Figure 3.2. Time histories of the centerline deflection of the flexible sheet at (a) U = 4.3 mm/s, (b) U = 7.15 mm/s, and (c) U = 11.44 mm/s.

other hand, the amplitude of the sheet oscillations increases linearly until it reaches a maximum at $U = 4$mm/s. Thereafter, with increasing flow velocity, the oscillation amplitude decays.

The time histories of these oscillations at specific flow rates have been presented in Fig. 3.2. At $U = 4.3$mm/s, where the structure has begun to oscillate, the flexible sheet stretches slowly with the slope at 0.17mm/s until a failure in the elastic fluid stresses in its wake cause the flexible sheet to recoil abruptly and the decay slope is considerably quicker at 2mm/s. As the flow rate is increased, the oscillations of the flexible sheet increases in frequency with its stretching rate increasing to 0.47mm/s at $U = 7.15$mm/s. The rate at which the flexible sheet recoils continues to be at 2mm/s. With increased flow rates, the oscillations of the flexible sheet continue to become

21
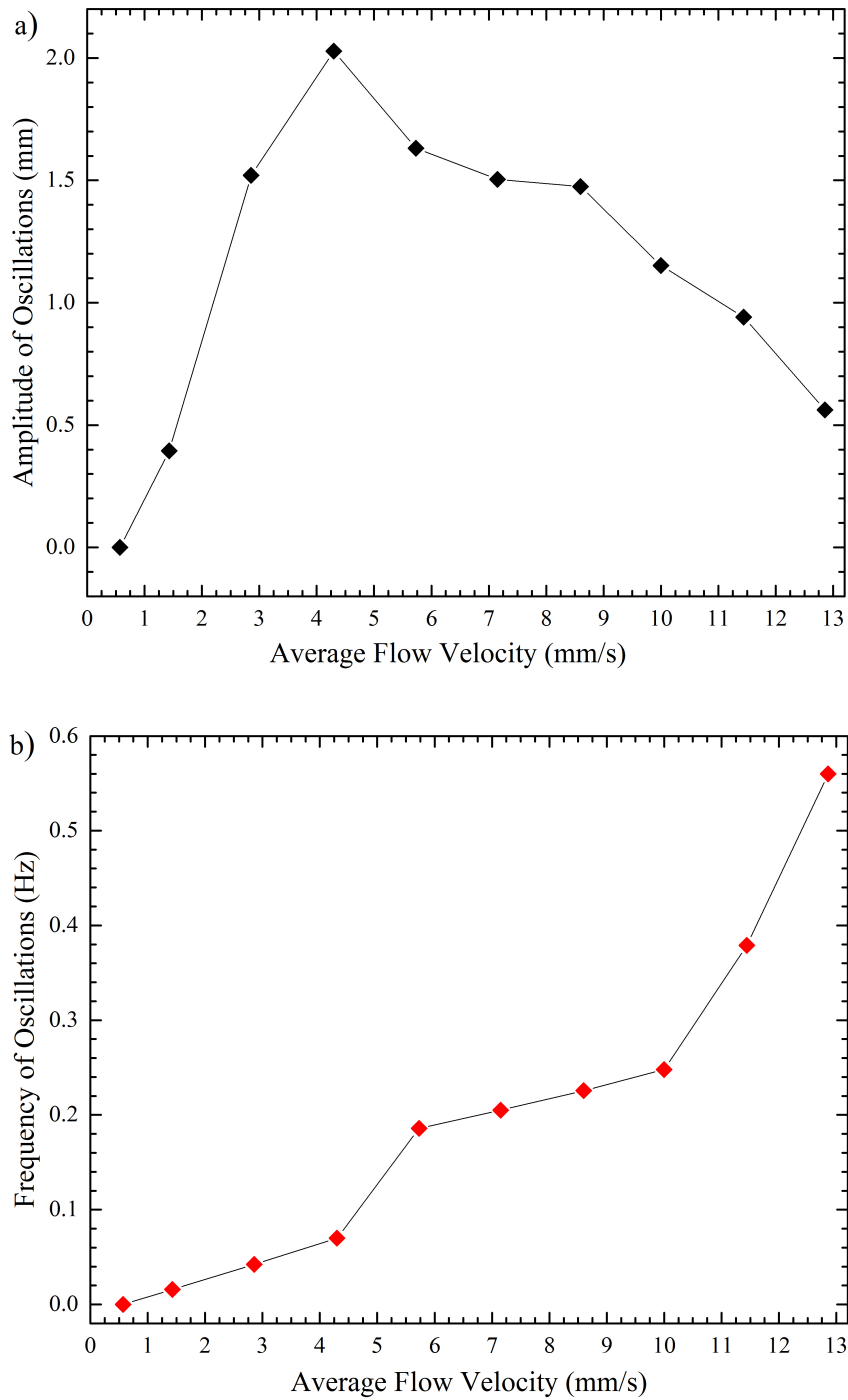
Figure 3.3. The (a)amplitude and (b)frequency of the flexible sheet oscillations plotted as a function of the flow velocity

22

more repetitive and it has a faster stretching rate of 0.68 mm/s at $U = 11.44$mm/s. The recoil rate of the flexible sheet stays the same. The oscillations of the flexible sheet at this flow rate and beyond become very chaotic and seem to show higher harmonics.

Another important observation from the time history plots of the flexible sheet is the smoothness of the displacement curve. At the lower flow rate of 4.3mm/s, the stretching of the flexible sheet is not uniform. There are minor peaks on the way of reaching the maximum displacement point in the oscillation cycle. These minor peaks may signify an instability of the flexible sheet at distant sections along its span. With the flow rate increasing to 7.15mm/s, the stretching of the sheet is smoother and the time history curve is a well-defined saw-tooth pattern. The higher frequency oscillations occurring at flow rates of 10mm/s and beyond, show a non-uniform pattern of peaks with no definite minimum and maximum displacement point in oscillation cycles.

At low flow velocities, the sheet is able to fully recoil before any significant extensional stress can be rebuilt in the wake. This results in a smooth deflection of the flexible sheet with a sudden and dramatic recoil of the sheet leading upto a maximum amplitude. Subsequently, with increasing flow velocity, the deformation rate of the flexible sheet also increases and becomes comparable to the recoil rate of the sheet. At this point, the flexible sheet does not achieve a complete recoil since the recoil rate is not faster than the growth of extensional stresses in the wake of the flexible sheet anymore. As a result, the amplitude of oscillations can be observed to decay with increasing flow velocity. Secondly, once the flow velocity gets beyond U_{crit}, the rapid recoil of the flexible sheet is found to occur due to a centralized breakdown of extensional stress in the wake of the sheet. However, this phenomenon does not stay the same at higher flow velocities. When the deformation rate and recoil rate of the sheet become comparable, the breakdown of extensional stresses in the wake

23

shifts from a global to a local phenomenon. As a result, local breakdowns in the fluid extensional stress at various regions along the span of the flexible sheet begin to dominate which effectively decrease amplitude of oscillations while increasing the frequency as seen in Fig. 3.4.
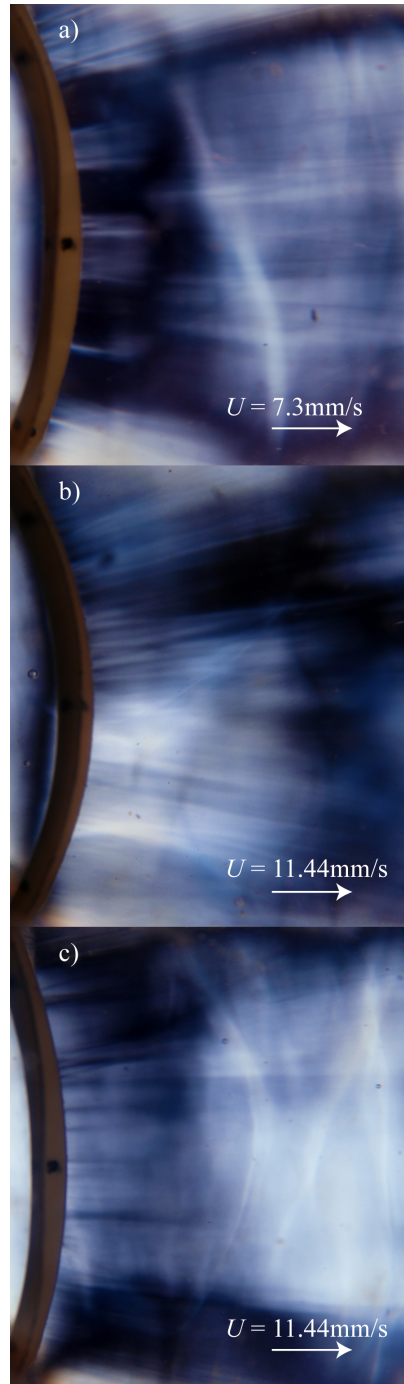
Figure 3.4. The bright and dark regions in the wake of the flexible sheet in the images seen above highlight the different states of extensional fluid stresses. In (a), at a lower flow velocity $U = 7.3$mm/s, the stresses developed are uniform as seen by the uniformly dark area in the image. At a higher flow velocity shown in (b) and (c), the extensional stresses are not uniform as seen by the irregular bright and dark regions along the span in the wake of the flexible sheet.

25

| Light source | Polarizer at 45° | Flow cell | Polarizer at 135° | Camera |
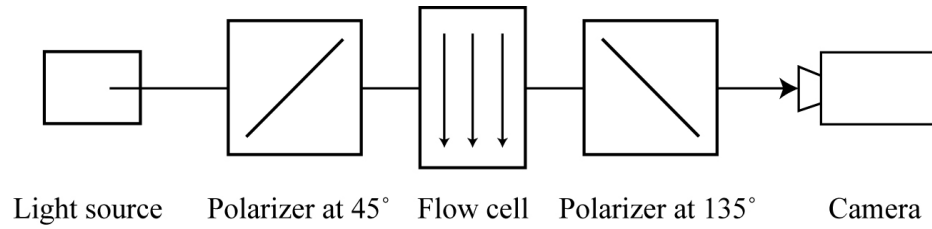
Figure 3.5. Schematic diagram of the setup used to obtain flow induced birefringence images in this study

3.2   Flow-induced birefringence (FIB)

Full-field flow-induced birefringence measurements were made using the crossed polarizer technique described in [54]. The areas of large micellar deformation are clearly seen in Fig. 3.6 at a flow velocity of $U = 4.3mm/s$. The polarizers have been oriented at 45° and 135° and the regions of extensional deformation are highlighted. It is known that in flows with stagnation points, that that a narrow region of high polymer or micelle deformation known as birefringent strands can form in the strong extensional flow just downstream of the stagnation point [55,56]. These birefringent strands appear as bright areas or fringes directly in the wake of the flexible sheet. These fringe patterns are in excellent agreement with the patterns observed in both experiments [57] and numerical simulations [58,59].In Fig. 3.6, the birefringence quickly goes through orders, here seen as rainbow fringe patterns, indicating a substantial amount of deformation and thus stress accumulated by the fluid as it flows past the flexible sheet. Because of this, it is impossible as a practical matter to obtain a quantitative value of the extinction and retardation angles from which to calculate a value of stress. Additionally, under such large deformations, the linear stress-optic rule no longer holds, and thus the birefringence data is used only as a qualitative tool to guide the eye. However, it is still qualitatively an excellent tool to examine the stress and deformation fields generated by the flow around the flexible sheet during its time-dependent fluctuations.
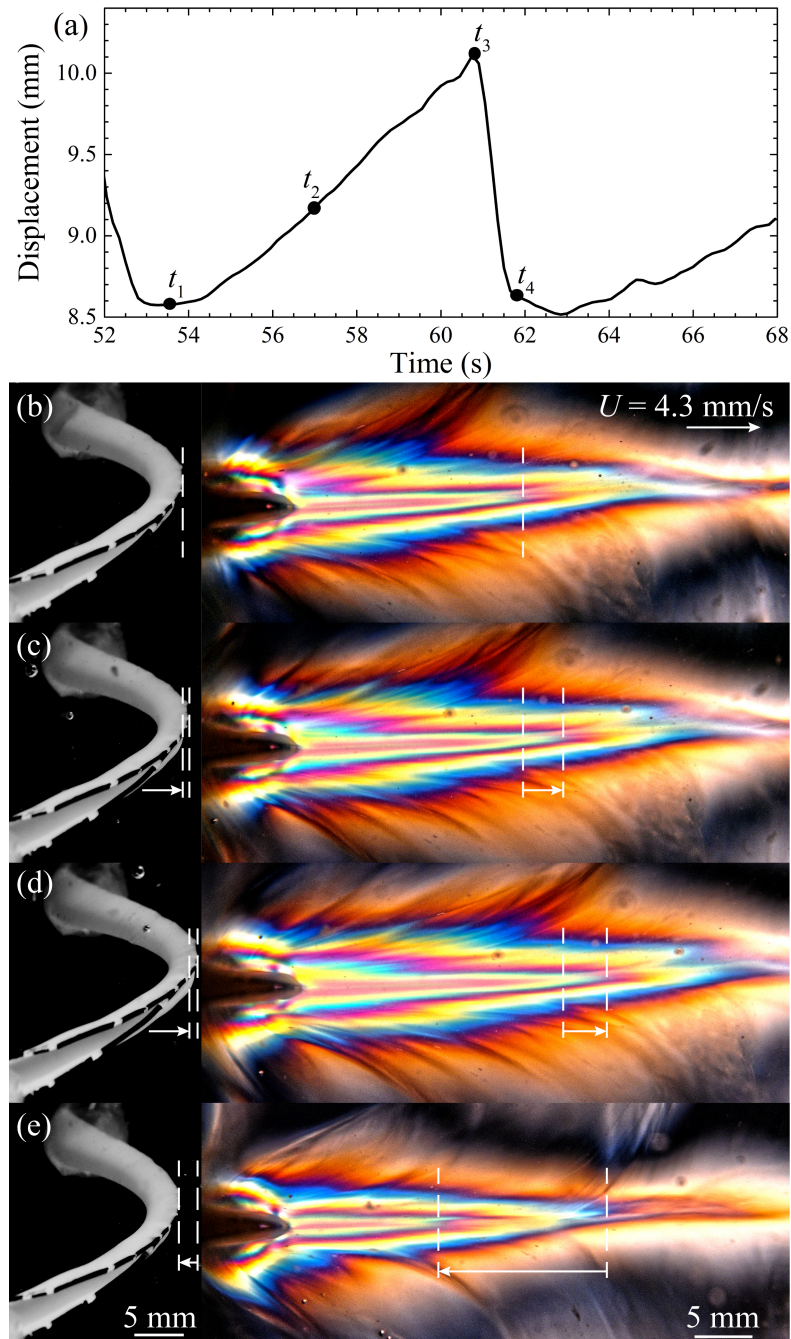
Figure 3.6. (a) Time history of the centerline deflection of the sheet for one period of oscillation, together with bright field images of deformed sheet (left), and the extensional birefringent patterns obtained by setting the crossed polarizers at 45° and 135° (right) at $U = 4.3$ mm/s and for (b) $t_1 = 0$, (c) $t_2 = 3.45$ s, (d) $t_3 = 7.2$ s, and (e) $t_4 = 7.95$ s. The dashed lines highlight the difference in the extensional birefringence patterns and deformations of the sheet between each time interval.

27

As seen in Fig. 3.6, a narrow region of micelle deformation, known as a birefringent tail, forms in the strong extensional flow region just downstream of the stagnation point. In the wake, the fluid must accelerate from rest along the trailing edge of the sheet to the maximum flow velocity U_{max} over a short distance downstream of the flexible sheet. This extensional flow results in strong micelle alignment and deformation as seen in Fig. 3.6(b). As the flow velocity is increased, a stable birefringence tail grows both in length and intensity until the onset of the viscoelastic flow instability. After the onset of the flow instability, the maximum extent of the birefringent tail approaches an asymptotic limit. A series of dashed lines have been added to Fig. 3.6 to graphically illustrate the magnitude and direction of the changes to the birefringence pattern with time during one oscillation cycle. A similar line has been added to show the deflection of the sheet in the bright-field images to the left of the FIB. At the start of an oscillation (Fig. 3.6(b)), the wormlike micelle solution already exhibits a significant amount of extensional stress in its wake. The birefringent tail grows in length and intensity with time (Fig. 3.6(c)) resulting in still further stretching of the flexible sheet. At its maximum extent (Fig. 3.6(d)), the birefringence has grown by approximately 30% beyond its minimum extent (Fig. 3.6(b)) to nearly $10H$ downstream, while the deflection of the sheet has increased by roughly 12% from 8.5 mm to 10 mm. When the displacement of the sheet reaches 10 mm, an abrupt breakdown of the wormlike micelles in the high stress wake is observed resulting in a rapid loss of extensional stress in the wake. This can be seen in Fig. 3.6(e) as a significant reduction in the length and extent of the birefringent tail. The start of the next oscillatory cycle corresponds to the flow of new unaffected wormlike micelles from upstream of the flexible sheet into its wake where they begin to stretch and deform the flexible sheet again. Similar FIB patterns were observed at all flow velocities where the flow of wormlike micelle solution was found to become unstable.
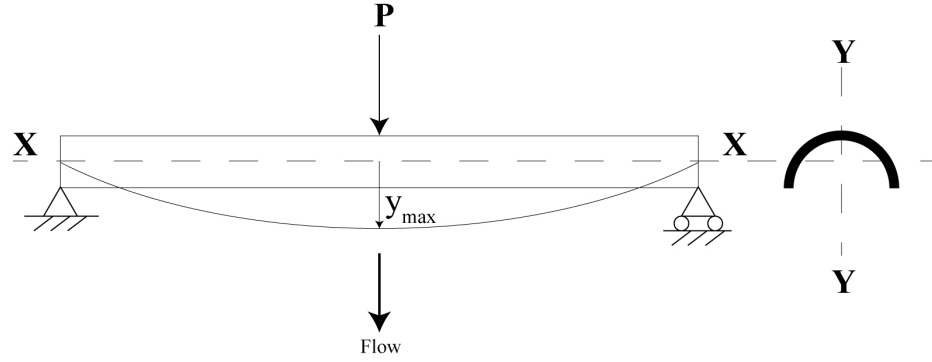
Figure 3.7. The spanwise deformation of the flexible sheet during the oscillation cycle

3.3   Flexible sheet deformation and extensional fluid stresses

It can observed that the flexible sheet does not only undergo a span wise deformation but also a complex 'C' shaped curvature seen in the cross section. Thus, in order to correlate the extensional stress developed in the fluid in the wake to the total stress applied on the flexible sheet, it is important to take into consideration the total deformation of the flexible sheet in-line and also cross-flow to the flow direction. To simplify calculations, we have estimated the stress experienced by the flexible sheet in separate cases, that is, in the in-line and cross-flow directions, even though the resulting deformation occurs simultaneously and thus is quite a complex occurrence. The stress required for the in-line sheet deformation can be calculated by assuming the sheet to be a simply supported beam with a 'C' cross section profile and using Euler's beam theory to estimate the maximum force applied in the midsection at the maximum observed displacement of the sheet. Thus, the force at the midsection of the flexible sheet for only in-line deformation is given by,

$$P = y_{max}\frac{48EI}{L^3} \tag{3.2}$$

where P is the load acting on the midsection, $y_{max} = 11mm$ is the maximum midsection flexible sheet displacment, $E = 0.1 \times 10^6 Pa$ is the elastic modulus of the flexible

29
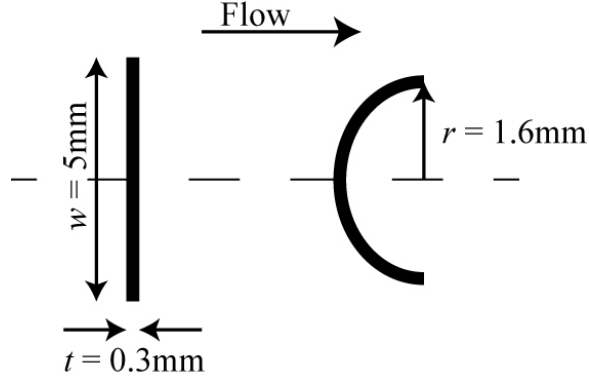
Figure 3.8. The assumed semi-circular cross section profile of the flexible sheet during the oscillation cycle

sheet and $I = 0.48mm^4$ is the second area moment of inertia of the 'C' shaped cross section of the flexible sheet. Thus, the stress experienced due to an in-line force acting on the flexible sheet can be found,

$$\tau_{inline} = \frac{P}{L \times B} = 5Pa \tag{3.3}$$

where $L \times B$ is the area of the flexible sheet exposed to the incoming flow. In addition to bending, there is a tensile stress which results from the sheet stretching from its initial undeformed state to its deformed elongated contour length at maximum deflection. By calculating the strain, ε, from the images of the deformed sheets, this stress was found to be approximately $\sigma_{tensile} = E\varepsilon = 13kPa$.

The stress required to bend the flexible sheet cross section into a 'C' profile results in a tensile elastic force acting on the outer layer of the sheet. This tensile stress on the flexible sheet is estimated below,

$$\text{Distance from neutral axis, } c = 0.15\,mm$$

$$\varepsilon_{neutral} = \frac{c}{r} = \frac{0.15\,mm}{1.6\,mm},$$

30

$$\tau_{crossflow} \; = \; E \, \varepsilon_{neutral} \; = \; 9 \, kPa \qquad (3.4)$$

From filament stretching extensional rheology measurements, the wormlike micelle solution was found to rupture and fail at an extensional stress of 7 kPa. Thus, these calculations appear to confirm that the viscoelastic fluidic stresses needed to deform the sheet are large enough to result in breakdown of viscoelastic wormlike micelles in the wake of the sheet, resulting in a time-dependent flow field, which in turn drives the observed time-dependent oscillations of the sheet. It is important to note that this is a simplified explanation of the oscillation mechanism. As the cross flow and inline deformation occur together, it can lead to changes in the sheet properties like the area moment of inertia and the cross section of the flexible sheet does not stay a 'C' shape across the sheet span throughout a period of oscillation.

CHAPTER 4

MODIFYING FLEXIBLE SHEET INCLINATION

4.1   Sheet displacement time histories

An additional set of experiments was conducted over the same range of Reynolds numbers for cases wherein the flexible sheet was placed at 0°, 20° and 45° to the flow direction. The desired inclination of the flexible sheet was achieved through external rotation of the fixtures holding the flexible sheet inside the flow cell. The 0° orientation did not oscillate for the range of flow rates tested and, as a result, discussion of the 0° case will not be included in the subsequent text. The centerline deflection of the flexible sheet for three different inclination angles tested is shown in Fig. 4.1(a). For completeness and ease of comparison, the data for the 90° case has been included in all subsequent figures. The side views of the complex deformation that the flexible sheet underwent for each inclination angle are shown in inset images in Fig. 4.1. As the flow began, the 45° flexible sheet was deformed into the flow direction with its cross-section forming a 'C' shape that was significantly less deformed than that of the 90° case. Unlike the 90° case, the 'C' shape remained open for all the flow velocities tested and did not completely bend back onto itself. At a critical flow velocity of $U = 2.8$ mm/s, the wormlike micelle solution became unstable, and periodic oscillations of the flexible sheet started in the same manner previously observed for the 90° case. The centerline deflection of the 45° flexible sheet increased linearly with flow velocity up to a maximum value which was smaller than that observed for the 90° case. After reaching this maximum value at $U = 5.7$ mm/s, the centerline deflection decreased and approached a plateau at the higher flow velocities
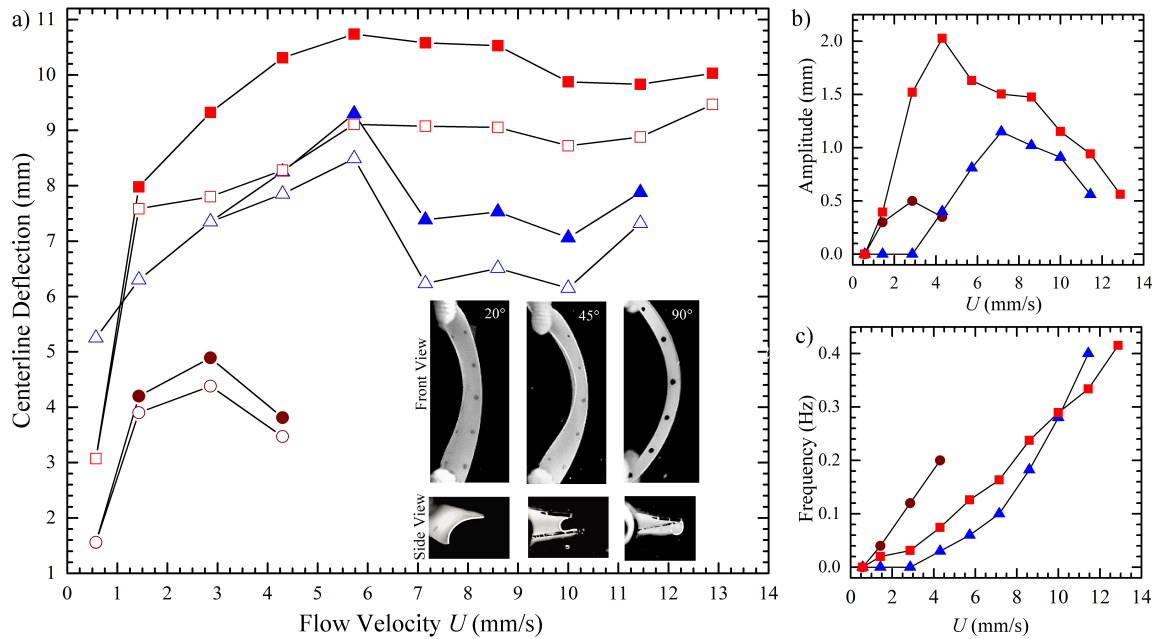
Figure 4.1. (a) Centerline displacement of the flexible sheet for 20°(●), 45°(▲) and 90°(■) inclinations. The filled and hollow symbols are used for the maximum and minimum flexible sheet displacements respectively during oscillations at each flow velocity. The inset contains the side views of the cross-flow deformation of the flexible sheet. (b, c) Amplitude and frequency of oscillations of the flexible sheet over the range of flow velocities tested. The error margin for the amplitude of oscillations is less than 10% for flow velocities below 4mm/s and less then 5% for higher flow velocities. The error margin is less than 5% for the frequency plots.

tested. For the 20° inclination, the flexible sheet began from a position aligned almost completely with the flow and the resulting cross section profile of the sheet had a much smaller curvature (Fig. 4.1(a)). The centerline deflection of the sheet was much smaller than the 45° and 90° cases with a maximum deflection of 5 mm compared to nearly 11 mm for the 90° case. For flow velocities larger than $U = 4.8$ mm/s, the 20° flexible sheet did not continue to hold the stretched deformation seen in Fig. 4.1(a), but instead rotated off the centerline where it remained in an asymmetric position closer to one of the side walls for the rest of the flow velocities tested and exhibited no further large-amplitude fluctuations. Data for the 20° case beyond $U = 4.8$ mm/s are therefore not presented in Fig. 4.1 or any subsequent plot. The amplitude and frequency of oscillations from the centerline deflection time histories are mapped out in Fig. 4.1(b) and (c) respectively. The amplitude of oscillations initially increased roughly linearly with increasing flow velocity for all three inclinations tested and reached a maximum. Beyond this maximum, the amplitudes of all three angles began to decay with increasing flow velocity. The oscillation frequency increased with flow velocity for all three inclinations.

4.2 Flexible sheet deformation and recoil rates

From the sawtooth waveform of the centerline deflection time histories, it was clear that the flexible sheet stretches slowly before recoiling rapidly during each oscillation cycle. In Fig. 4.2(a), the deformation and recoil velocities of the flexible sheet during oscillations are presented as a function of flow velocity for all three inclinations. It can be observed that the deformation velocity curve followed a similar trend for all three inclinations over the range of flow velocities tested. The recoil velocities, on the other hand, were very different for the three inclination angles. The 90° inclination curve had the largest recoil velocity by almost a factor of three. This can likely be attributed to the flexible sheet recoil velocity being dependent on the elastic stress

34

built up within the sheet which is clearly at a maximum within the 90° sheet due to the increased sheet deformation at any given flow velocity. Conversely, the deformation velocity of the sheet is strongly dependent on the flow conditions as it is coupled to the convection of fluid from upstream of the sheet to rebuild elastic stress in the wake of the sheet after a fluid rupture event. As a result, as seen in Fig. 4.2(a), the deformation velocity is not strongly coupled to the sheet orientation. A plot of the ratio of deformation and recoil velocities of the flexible sheet over varying flow velocities is shown in Fig. 4.2(b). For the 45° and 90° inclination angles, the ratio of the deformation rate to recoil rate was found to start quite small at a value of less than 0.1 and then to increase with flow velocity to reach a plateau beyond $U = 8$ mm/s. This plateau of the ratio of deformation and recoil velocity corresponds to the point at which higher harmonics appear in the oscillations and the amplitude begins to decay. For the case of the 90° sheet, the ratios of deformation rate to recoil rate reached a plateau of just over 0.2. As such the dynamics of oscillation were dominated by the fast recoil of the sheet after fluid rupture. Conversely, this rate approached 0.6 for the 45° sheet resulting in a more symmetric oscillation cycle and a growth in deformation that nearly matched its decay. Although the 20° did not reach a plateau before twisting from the centerline, breaking symmetry and ceasing to oscillate, its behavior appears to be closer to that of the 45° sheet than the 90° sheet.

4.3 Non-dimensionalization of system variables

Finally, we concentrate on the results presented in the previous sections with the objective of combining the dimensional results from the different flexible sheet inclinations into a cohesive set of results using a single non-dimensional parameter. In order to collapse the data for all three inclination angles, a non-dimensional flow velocity, U^*, a non-dimensional oscillation amplitude, A^*, and a non-dimensional frequency, f^*, were considered. The non-dimensional velocity that best collapsed the

35
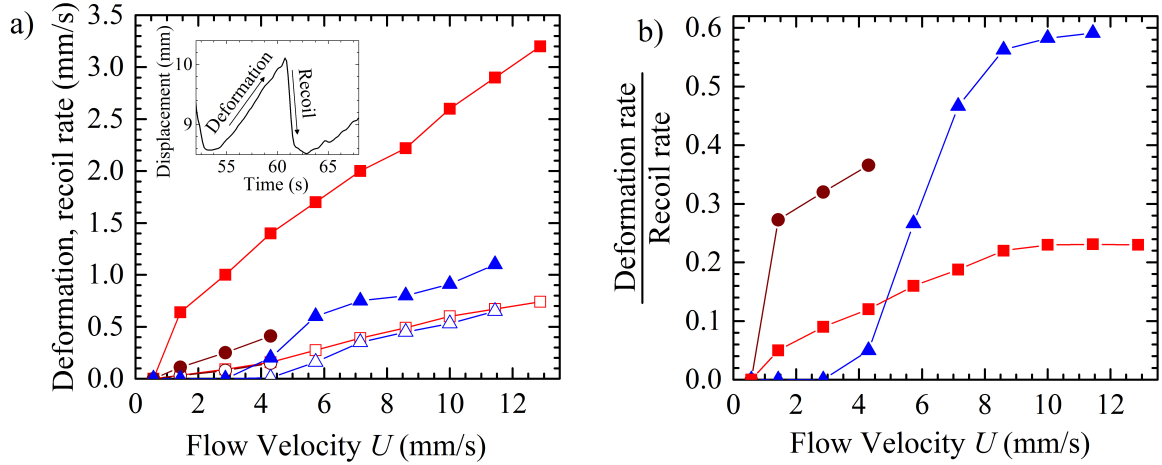
Figure 4.2. (a) The deformation rate (open symbols) and recoil rate (filled symbols) during an oscillation cycle for the flexible sheet aligned at a 20°(●), 45°(▲) and 90°(■) inclination to the flow direction as a function of flow velocity. (b) The ratio of deformation and recoil rates of the flexible sheet as a function of flow velocity for the three flexible sheet inclination angles.

data both in terms of the critical onset conditions and the flow velocity corresponding to the maximum oscillation amplitude was found to be $U^* = U/(w\sin(\theta)f_\theta)$. Here U is the flow velocity, w is the width of the flexible sheet, θ is the inclination angle of the sheet, $w\sin(\theta)$ is the equivalent surface area of the flexible sheet exposed to the flow, and f_θ is the frequency of oscillations at the critical flow velocity which depends on the inclination angle of the flexible sheet. As seen in Fig. 4.3(a), using this dimensionless velocity, both the onset condition and the maximum of the oscillation amplitude collapse to the values of $U^* \approx 7$ and $U^* \approx 42$, respectively. It is expected that the appropriate dimensionless velocity should also contain some information about the viscoelastic fluid properties, specifically, the relaxation time of the fluid, λ. However, because in this study only a single fluid composition was used, this hypothesis could not be fully tested. As seen in the inset in Fig. 4.3(b), a renormalization of the critical oscillation frequency with the relaxation time to form a modified Weissenberg number, $Wi_f = \lambda f_\theta$, appears to be a promising first step towards incorporating rheological information into our analysis as the value approaches $Wi_f \sim 1$. Future studies will
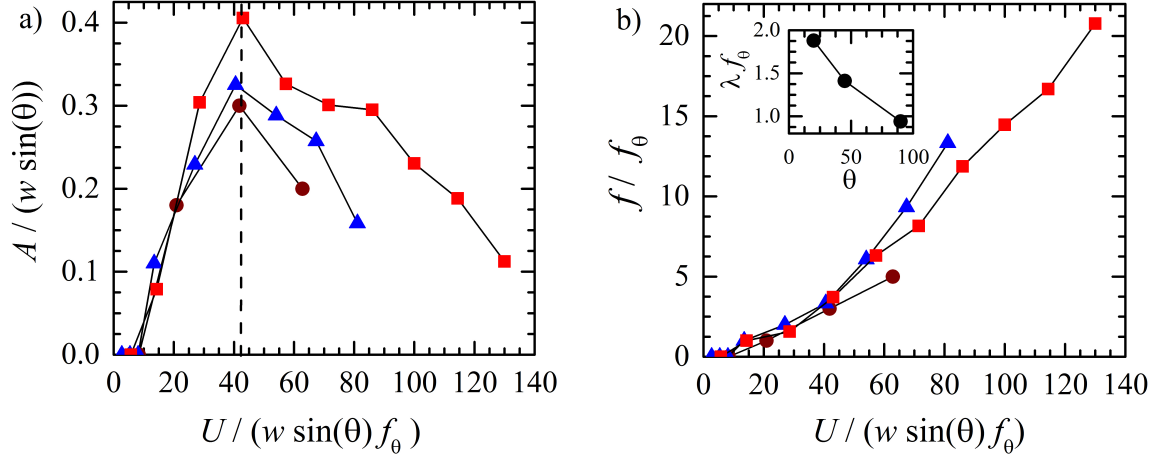
Figure 4.3. The dimensionless (a) amplitude and (b) frequency of oscillations as a function of the dimensionless flow velocity for flexible sheet inclination angles of $20°(\bullet)$, $45°(\blacktriangle)$ and $90°(\blacksquare)$. The inset in (b) contains the dimensionless product, λf_θ, as a function of inclination angle.

focus on how changes in fluid rheology affects the observed viscoelastic fluid-structure interactions. The appropriate non-dimensional amplitude and frequency were found to be $A^* = A/w\sin(\theta)$ and $f^* = f/f_\theta$, where A and f are the dimensional amplitude and frequency of flexible sheet oscillations, respectively. Using these dimensionless parameters, the data from the three inclination angles are collapsed onto a master curve as seen in Fig. 4.3(a) and (b). The slight variations in the data are likely the result of the complex deformation of the flexible sheet under flow. The deviation of scaling for higher flow velocities could be due to the higher harmonics that become dominant during oscillations.

37

CHAPTER 5

MODIFYING FLEXIBLE SHEET WIDTH

Another extension to this study that was investigated was the effect of modifying the flexible sheet width. The width of the flexible sheet was reduced from 5mm to 2.5mm while the experimental setup and range of flow velocities tested remained unchanged. After mounting the modified flexible sheet, the fixtures holding the ends of the sheet at the end walls were rotated to the required inclinations of 45° and 90°. The centerline deflection for the 45° and 90° modified flexible sheet inclinations tested is shown in Fig. 5.1(a). As the flow started, the flexible sheet was displaced into the flow direction as previously seen. The cross-flow deformation profile of the sheet can be viewed in the inset. Instead of forming a complete 'C' profile, the sheet was able to only bend slightly leading to an asymmetrical shape which was approximately half of a complete 'C' shape that was observed for the larger 5mm width flexible sheet. The centerline displacement of the 2.5mm width flexible sheet increased steadily with the flow velocity and reached a plateau at 3mm/s and 5.7mm/s for the 90° and 45° flexible sheet inclinations respectively. The amplitude and frequency of oscillations have been mapped out in Fig. 5.1(b) and (c). As observed for the 5mm width flexible sheet inclinations, the amplitude of oscillations increased to a maximum value and started to decay with increasing flow velocity while the frequency of oscillations increased monotonically with flow velocity. The critical velocity at which the unstable oscillations began was the same for both flexible sheet oscillations while the maximum amplitude was attained at $U = 2.8$ mm/s and $U = 4.3$ mm/s for the 90° and 45° flexible sheet oscillations respectively. As described in the previous section, the
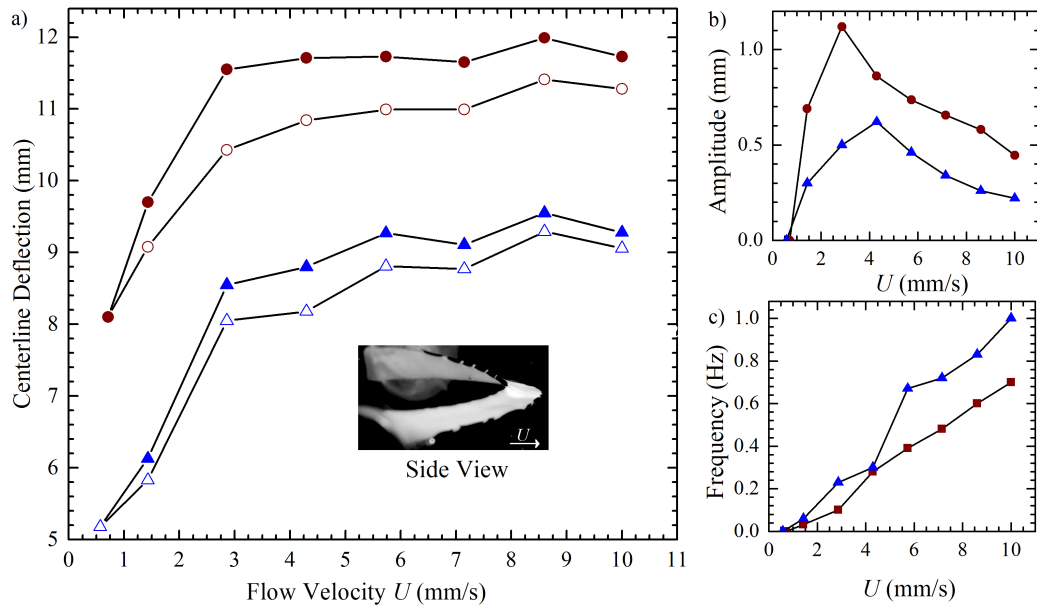
Figure 5.1. (a) Centerline displacement of the flexible sheet of width $w=$ 2.5mm for $90°(\bullet)$ and $45°(\blacktriangle)$ inclinations. The filled and hollow symbols are used for the maximum and minimum flexible sheet displacements respectively during oscillations at each flow velocity. The inset contains a side view of the cross-flow deformation of the flexible sheet. (b, c) Amplitude and frequency of oscillations of the flexible sheet over the range of flow velocities tested. The error margin for the amplitude of oscillations is less than 10% for flow velocities below 4mm/s and less then 5% for higher flow velocities. The error margin is less than 5% for the frequency plots.
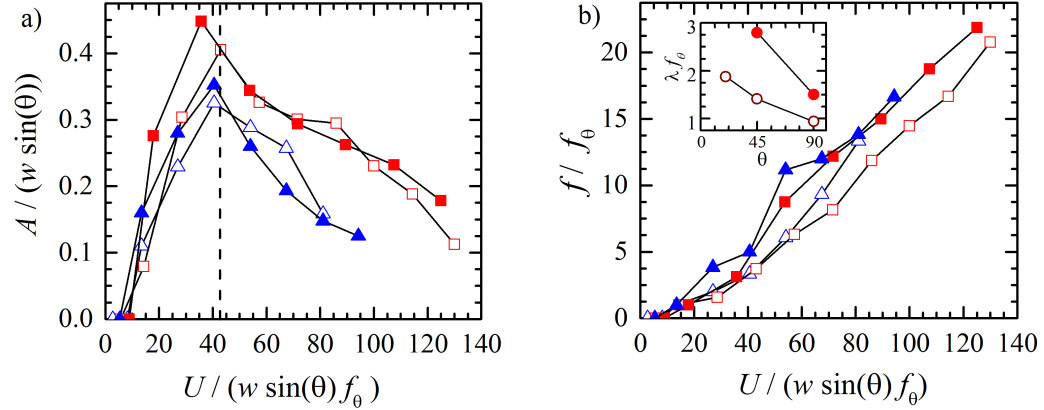
Figure 5.2. The dimensionless (a) amplitude and (b) frequency of oscillations as a function of the dimensionless flow velocity for flexible sheet inclination angles of 45°(▲) and 90°(■). The inset in (b) contains the dimensionless product, λf_θ, as a function of inclination angle. The filled and hollow symbols represent data for the flexible sheet width of 5mm and 2.5mm respectively.

observation of a global breakdown of wormlike micelles at low velocities transitioning to distributed local micellar breakdowns leading to higher harmonics were verified for the 2.5mm flexible sheet width inclinations. However, in addition, at high flow velocities, the 2.5mm flexible sheet was forced to align with the flow direction in the mid section area. This alignment of the flexible sheet profile differs from that observed for the 20° flexible sheet inclination at $w =$5mm as, in the latter case, the entire sheet span was inclined at 20° to the flow direction and with increasing flow velocity the entire sheet span became completely aligned with the flow and the unstable flexible sheet oscillations ceased to occur. For the 90° and 45° flexible sheet inclinations at $w =$2.5mm, the unstable oscillations continued to occur, however with decaying amplitude.

The non-dimensional amplitude and frequency of oscillations for the case of $w =$2.5mm have been plotted along with those of $w =$5mm at 90° and 45° flexible sheet inclinations in Fig. 5.2(a) and (b). It can be seen that the non-dimensional critical velocity, $U^* = 4.2$ remains applicable for this flexible sheet modification. The frequency of

oscillations too follows a similar trend. Thus, the non-dimensional analysis for this experimental setup has been effective at collapsing the data into a master curve.

CHAPTER 6

CONCLUSION

In this work, the results of an investigation into the existence of non-Newtonian fluid-structure interactions are presented. Fluid-structure interaction studies have until now only comprised of Newtonian fluids used as test fluids. In this study, we show that the elastic instabilities occurring during the flow of non-Newtonian fluids can also drive the motion of structures resulting in a new and as yet unexplored field of FSI studies. We use wormlike micelle solution as the non-Newtonian viscoelastic fluid flowing past a flexible elastic sheet. By systematically varying the flow velocity, flow kinematics, flexible sheet displacement and bifurcation diagram were obtained and used to characterize viscoelastic fluid-structure interactions.

For a stable flow velocity, the extensional stresses produced by the wormlike micelle solution in the wake of the flexible sheet produced a static deflection of the flexible sheet. Beyond a critical flow velocity, while at an infinitesimal Re, the fluid was found to show elastic instabilities, resulting in periodic fluctuating stresses in the wake of the flexible sheet. These periodic elestic instabilities have been observed in a number of studies using this test fluid [14,54,60]. However, in this study, these elastic instabilities occur in the wake of a flexible sheet which imparts a periodic fluctuating stress on the structure too. The flexible sheet was found to have periodic oscillations with a saw tooth-like pattern seen in a time history plot. A bifurcation diagram is presented to show the progression of the amplitude of the flexible sheet oscillation about its mean center-line deflection. From the amplitude and frequency plots, it is found that amplitude of oscillations grows linearly until a maximum, after

which it plateaus and then decays with increasing flow velocity while the frequency of oscillations is always increasing monotonically with increasing flow velocity. This trend has been attributed to the varying difference between the growth rate of stresses in the fluid which is dependent on the flow velocity and the recoil rate of the flexible sheet which is a structural property. Along with this transition comes the change in the dominance of local fluid elastic instabilities instead of a global central instability with increasing flow velocity.

Flow induced birefringence images show the transition of slow growth and rapid decay of extensional stresses in the wake of the flexible sheet in terms of the changing length and intensity of the birefringent tail observed in the wake. Additionally, there is no vortex shedding observed during the oscillation cycles as is common in Newtonian FSI studies. The complex deformation that the flexible sheet undergoes during each cycle of oscillation has been highlighted in the bright field images. These images indicate the inline and cross-flow deformation that occur simultaneously with increasing extensional stresses produced by the fluid flowing past the sheet.

An analysis of the stresses required to produce the sheet deformation has been conducted in order to correlate the extensional stress in the fluid with the stresses required to produce the observed deformation of the flexible sheet. It has been shown that the tensile stress needed for the in-line stretching of the flexible sheet and the stress needed to bend the cross section of the flexible sheet into a complex 'C' shape is many times greater than that required for the in-line bending of the sheet span. These stresses are found to be close to the magnitude of the maximum elastic normal stresses that can be supported by the fluid before the stretched and deformed micelles in the solution fail(2.4.3). We are able to conclude that there is a strong relation between the observed magnitude of flexible sheet deformation and the maximum elastic tensile stresses reached before filament failure studied through filament stretching extensional rheology measurements performed on this solution.

43

In conclusion, we have shown, for the very first time, that purely elastic flow instabilities occurring in a viscoelastic fluid flow can drive the motion of a flexible structure placed in its path. The oscillations of the flexible structure, which develop at infinitesimal Reynolds numbers and in the absence of vortex shedding, have been presented for three inclinations and two width variations of a flexible sheet. The measurements of the structural deformation velocity profiles and the FIB have been used to quantify the time variation of the flow field and the state of stress in the fluid during the oscillations. These results have been further classified using a set of proposed non-dimensional parameters. These observations open up an entirely new field of study. The results from this work relating to the three flexible sheet inclinations have been published in the Journal of Fluid Mechanics [61].

BIBLIOGRAPHY

[1] P. Flory, *Principles of Polymer Chemistry*. Ithaca: Cornell University Press, 1953.

[2] V. Anderson, J. Pearson, and E. Boek, "The rheology of worm-like micellar fluids," in *Rheology Reviews*, D. Binding and K. Walters, Eds. The British Society of Rheology, 2006, vol. 4, pp. 217–253.

[3] S. Kefi, J. Lee, T. Pope, P. Sullivan, E. Nelson, A. Hernandez, T. Olsen, M. Parlar, B. Powers, A. Roy, A. Wilson, and A. Twynam, "Expanding applications for viscoelastic surfactants," *Oilfield Review*, pp. 10–16, 2004.

[4] J. Zakin and H. Bewersdorff, "Surfactant drag reduction," *Rev. Chem. Eng.*, vol. 14, no. 45, pp. 253–320, 1998.

[5] J. N. Israelachvili, *Intermolecular and surface forces: with applications to colloidal and biological systems*. London: Academic Press, 1985.

[6] R. G. Larson, *The Structure and Rheology of Complex Fluids*. New York: Oxford University Press, 1999.

[7] H. Rehage and H. Hoffmann, "Viscoelastic surfactant solutions: model systems for rheological research," *Mol. Phys.*, vol. 74, no. 5, pp. 933–973, 1991.

[8] P. Schurtenberger, R. Scartazzini, L. Magid, M. Leser, and P. Luisi, "Structural and dynamic properties of polymer-like reverse micelles," *J. Phys. Chem.*, vol. 94, no. 9, pp. 3695–3701, 1990.

[9] S.-H. Tung, Y.-E. Huang, and S. Raghavan, "A new reverse wormlike micellar system: Mixtures of bile salt and lecithin in organic liquids," *J. Am. Chem. Soc.*, vol. 128, pp. 5751–5756, 2006.

[10] R. Laughlin, *The Aqueous Phase Behavior of Surfactants*. New York: Academic Press, 1994.

[11] J. Appell, G. Porte, A. Khatory, F. Kern, and S. Candau, "Static and dynamic properties of a network of wormlike surfactant micelles (etylpyridinium chloride in sodium chlorate brine)," *J. Phys. II*, vol. 2, pp. 1045–1052, 1992.

[12] J. P. Rothstein, "Transient extensional rheology of wormlike micelle solutions," *Journal of Rheology*, vol. 47, no. 5, pp. 1227–1247, 2003.

[13] A. Bhardwaj, E. Miller, and J. P. Rothstein, "Filament stretching and capillary breakup extensional rheometry measurements of viscoelastic wormlike micelle solutions," *Journal of Rheology*, vol. 51, no. 4, pp. 693–719, 2007.

[14] S. Chen and J. P. Rothstein, "Flow of a wormlike micelle solution past a falling sphere," *Journal of Non-Newtonian Fluid Mechanics*, vol. 116, no. 23, pp. 205 – 234, 2004.

[15] J. R. Gladden and A. Belmonte, "Motion of a viscoelastic micellar fluid around a cylinder: Flow and fracture," *Phys. Rev. Lett.*, vol. 98, no. 22, p. 224501, 2007.

[16] P. W. Bearman, "Vortex shedding from oscillating bluff bodies," *Annu. Rev. Fluid Mech.*, vol. 16, no. 1, pp. 195–222, 1984.

[17] R. D. Blevins, *Flow-induced vibration.* Krieger Pub. Co., Malabar, Fla., 1990.

[18] M. P. Païdoussis, S. J. Price, and E. de Langre, *Fluid-Structure Interactions - Cross-Flow-Induced Instabilities.* Cambridge University Press, New York, 2011, vol. 1.

[19] M. P. Païdoussis, *Fluid-Structure Interactions: Slender Structures and Axial Flow, Vol. 1.* San Diego, CA: Academic Press Inc, 1998.

[20] M. Païdoussis, *Fluid-Structure Interactions: Slender Structures and Axial Flow, Vol. 2.* Academic Press, London, 2004.

[21] C. Williamson and R. Govardhan, "Vortex-induced vibrations," *Annu. Rev. Fluid Mech.*, vol. 36, pp. 413–455, 2004.

[22] T. Sarpkaya, "A critical review of the intrinsic nature of vortex-induced vibrations," *J. Fluids and Struct.*, vol. 19, no. 4, pp. 389 – 447, 2004.

[23] P. Bearman, "Circular cylinder wakes and vortex-induced vibrations," *Journal of Fluids and Structures*, vol. 27, no. 56, pp. 648 – 658, 2011.

[24] A. Ongoren and D. Rockwell, "Flow structure from an oscillating cylinder part 1. mechanisms of phase shift and recovery in the near wake," *Journal of Fluid Mechanics*, vol. 191, no. 1, pp. 197–223, 1988.

[25] J. Carberry, J. Sheridan, and D. Rockwell, "Controlled oscillations of a cylinder: forces and wake modes," *Journal of Fluid Mechanics*, vol. 538, pp. 31–70, 2005.

[26] J. S. Leontini, B. E. Stewart, M. C. Thompson, and K. Hourigan, "Wake state and energy transitions of an oscillating cylinder at low reynolds number," *Physics of Fluids (1994-present)*, vol. 18, no. 6, pp. –, 2006.

[27] T. Prasanth and S. Mittal, "Vortex-induced vibrations of a circular cylinder at low reynolds numbers," *Journal of Fluid Mechanics*, vol. 594, p. 463, 2008.

[28] D. Jeon and M. Gharib, "On circular cylinders undergoing two-degree-of-freedom forced motions," *Journal of Fluids and Structures*, vol. 15, no. 3, pp. 533–541, 2001.

[29] N. Jauvtis and C. Williamson, "The effect of two degrees of freedom on vortex-induced vibration at low mass and damping," *Journal of Fluid Mechanics*, vol. 509, no. 6, pp. 23–62, 2004.

[30] J. M. Dahl, F. S. Hover, M. S. Triantafyllou, S. Dong, and G. E. Karniadakis, "Resonant vibrations of bluff bodies cause multivortex shedding and high frequency forces," *Phys. Rev. Lett.*, vol. 99, p. 144503, Oct 2007.

[31] J. Dahl, F. Hover, M. Triantafyllou, and O. Oakley, "Dual resonance in vortex-induced vibrations at subcritical and supercritical reynolds numbers," *Journal of Fluid Mechanics*, vol. 643, no. 1, pp. 395–424, 2010.

[32] A. Trim, H. Braaten, H. Lie, and M. Tognarelli, "Experimental investigation of vortex-induced vibration of long marine risers," *Journal of fluids and structures*, vol. 21, no. 3, pp. 335–361, 2005.

[33] J. K. Vandiver, V. Jaiswal, and V. Jhingran, "Insights on vortex-induced, traveling waves on long risers," *Journal of Fluids and Structures*, vol. 25, no. 4, pp. 641–653, 2009.

[34] Y. Modarres-Sadeghi, H. Mukundan, J. Dahl, F. Hover, and M. Triantafyllou, "The effect of higher harmonic forces on fatigue life of marine risers," *Journal of Sound and Vibration*, vol. 329, no. 1, pp. 43 – 55, 2010.

[35] R. Bourguet, G. E. Karniadakis, and M. S. Triantafyllou, "Distributed lock-in drives broadband vortex-induced vibrations of a long flexible cylinder in shear flow," *Journal of Fluid Mechanics*, vol. 717, pp. 361–375, 2013.

[36] G. H. McKinley, P. Pakdel, and A. Oztekin, "Rheological and geometric scaling of purely elastic flow instabilities," *J. Non-Newtonian Fluid Mech.*, vol. 67, pp. 19–47, 1996.

[37] K. Takeuchi, Y. Majima, K. Hirata, A. Morishita, M. Hattori, and Y. Sakakura, "Viscoelastic properties of middle ear effusions from pediatric otitis media with effusion and their relation to gross appearance," *European Archives of Oto-Rhino-Laryngology*, vol. 247, no. 1, pp. 60–62, 1990.

[38] E. Lauga, "Life at high deborah number," *EPL*, vol. 86, p. 64001, 2009.

[39] J. Teran, L. Fauci, and M. Shelley, "Viscoelastic fluid response can increase the speed and efficiency of a free swimmer," *Phys. Rev. Lett.*, vol. 104, p. 03801, 2010.

[40] B. Liu, T. Powers, and K. S. Breuer, "Force-free swimming of a model helical flagellum in viscoelastic fluids," *PNAS*, vol. 108, no. 19516-19520, 2011.

[41] J. Espinosa-Garcia, E. Lauga, and R. Zenit, "Fluid elasticity increases the loco-motion of flexible swimmers," *Phys. Fluids*, vol. 25, p. 031701, 2013.

[42] J. Drappier, D. Bonn, J. Meunier, S. Lerouge, J. Decruppe, and F. Bertrand, "Correlation between birefringent bands and shear bands in surfactant solutions," *J. Stat. Mech. Theory and Exp.*, p. P04003, 2006.

[43] G. G. Fuller, *Optical Rheometry of Complex Fluids*. New York: Oxford University Press, 1995.

[44] T. Shikata, S. Dahman, and D. Pearson, "Rheo-optic behavior of wormlike micelles," *Langmuir*, vol. 10, pp. 3470–3476, 1994.

[45] E. Wheeler, P. Fischer, and G. Fuller, "Time-periodic flow induced structures and instabilities in a viscoelastic surfactant solution," *J. Non-Newtonian Fluid Mech.*, vol. 75, pp. 193–208, 1998.

[46] R. Bird, R. Armstrong, and O. Hassager, *Dynamics of Polymeric Liquids: Volume 1 Fluid Mechanics*. New York: John Wiley & Sons, 1987.

[47] P. Fischer and H. Rehage, "Rheological master curves of viscoelastic surfactant solutions by varying the solvent viscosity and temperature," *Langmuir*, vol. 13, pp. 7012–7020, 1997.

[48] M. Cates, "Reptation of living polymers: Dynamics of entangled polymers in the presence of reversible chain-scission reactions," *Macromol.*, vol. 20, pp. 2289–2296, 1987.

[49] R. Granek and M. Cates, "Stress relaxation in living polymers: Results from a poisson renewal model," *J. Chem. Phys.*, vol. 96, pp. 4758–4767, 1992.

[50] M. Doi and S. Edwards, *The Theory of Polymer Dynamics*. Oxford: Oxford University Press, 1986.

[51] A. Bhardwaj, D. Richter, M. Chellamuthu, and J. P. Rothstein, "The effect of preshear on the extensional rheology of wormlike micelle solutions," *Rheol. Acta*, vol. 46, no. 6, pp. 861–875, 2007.

[52] P. Szabo, "Transient filament stretching rheometry i: Force balance analysis," *Rheol. Acta*, vol. 36, pp. 277–284, 1997.

[53] S. L. Anna, G. H. McKinley, D. A. Nguyen, T. Sridhar, S. J. Muller, J. Huang, and D. F. James, "An inter-laboratory comparison of measurements from filament stretching rheometers using common test fluids," *J. Rheol.*, vol. 45, no. 1, pp. 83–114, 2001.

[54] G. R. Moss and J. P. Rothstein, "Flow of wormlike micelle solutions past a confined circular cylinder," *Journal of Non-Newtonian Fluid Mechanics*, vol. 165, no. 2122, pp. 1505 – 1515, 2010.

[55] R. Cressely and R. Hocquart, "Localized flow birefringence induced in the wake of obstackles," *Optica Acta*, vol. 27, no. 5, pp. 699–711, 1980.

[56] C. Chen and G. Warr, "Light scattering from wormlike micelles in an elongational flow," *Langmuir*, vol. 13, pp. 1374–1376, 1997.

[57] F. P. T. Baaijens, S. Selen, H. P. W. Baaijens, G. W. M. Peters, and H. E. H. Meijer, "Viscoelastic flow past a confined cylinder of a low density polyethylene melt," *J. Non-Newtonian Fluid Mech.*, vol. 68, pp. 173–203, 1997.

[58] M. Chilcott and J. Rallison, "Creeping flow of dilute polymer-solutions past cylinders and spheres," *J. Non-Newtonian Fluid Mech.*, vol. 29, pp. 381–432, 1988.

[59] A. Afonso, M. A. Alves, F. T. Pinho, and P. J. Oliveira, "Uniform flow of viscoelastic fluids past a confined falling cylinder," *Rheol. Acta*, vol. 47, pp. 325–348, 2008.

[60] G. R. Moss and J. P. Rothstein, "Flow of viscoelastic wormlike micelle solutions through a periodic array of cylinders," *J. Non-Newtonian Fluid Mech.*, vol. 165, pp. 1–13, 2010.

[61] A. A. Dey, Y. Modarres-Sadeghi, and J. P. Rothstein, "Experimental observation of viscoelastic fluidstructure interactions," *Journal of Fluid Mechanics*, vol. 813, 2017.